Robotica (2014) volume 32, pp. 985–1004. © Cambridge University Press 2013
doi:10.1017/S0263574713001161

A new geometry-based plan for inserting flexible needles to reach multiple targets

Oleg A. Bobrenkov†, Jaeyeon Lee‡ and Wooram Park†*

†*Department of Mechanical Engineering, The University of Texas at Dallas, Richardson, TX 75080, USA*
‡*Department of Electrical Engineering, The University of Texas at Dallas, Richardson, TX 75080, USA*

(Accepted November 14, 2013. First published online: December 16, 2013)

SUMMARY
The tip of a flexible needle with a bevel tip approximately follows a planar arc when it is inserted into soft tissue only with the force applied to the needle along the needle axis. The direction of the arc can be controlled by the rotation input around the needle axis. This flexible and steerable needle has been shown to have a considerable potential in clinical applications due to its maneuverability and steerability. Beyond the needle insertion to a single destination, this paper concerns obtaining needle trajectories that reach *multiple* targets. Specifically, we propose an algorithm for the insertion of a flexible needle to travel from a single insertion point (i.e. port) to multiple targets. The insertion is motivated by the observation that multiple targets can be reached by the flexible needle through a combination of insertion, partial retraction, turning, and reinsertion of the flexible needle. In this paper we develop an insertion algorithm that minimizes tissue damage during the needle insertion to multiple targets. To this end, a cost function which computes the length of needle trajectory that can be thought of as the tissue damage is defined, and is minimized. Through the minimization, we find the optimal insertion parameters such as the port location, the insertion direction at the port, the targeting order, the turning angles, and the lengths of forward insertions and retractions. To reduce the computation time, we perform workspace analysis for this approach to filter out the no-solution cases. We present numerical examples of the simulated needle insertion for multiple targets with and without obstacles and show the benefit of the proposed method in terms of the tissue damage and the number of skin punctures. Extensions of the proposed approach to more complex cases such as more than three target points and maneuvering around spherical obstacles are also discussed.

KEYWORDS: Medical robots and systems; Path planning; Motion planning; Novel applications of robotics; Surgical robots.

1. Introduction

For some percutaneous medical procedures, multiple locations should be targeted, resulting in multiple needle insertions. When multiple liver samples are to be obtained, multiple needle insertions should be performed for different targets in liver biopsy.[18] In brachytherapy for prostate cancer, implanting multiple radioactive seeds in the prostate requires many needle insertions.[6] Even though the multiple targets can be reached by multiple independent insertions of a needle, the insertion strategy can be improved in terms of tissue damage, pain, and infection. As conceptually shown in Fig. 1 of Reed *et al.*,[24] two target points in tissue can be reached by a steerable flexible needle from a single insertion point. This is possible through initial insertion, partial retraction, turning, and reinsertion. This brings less tissue damage than multiple new insertions. In addition, since only one skin puncture is involved, the pain by the puncture is less than that by multiple punctures. Even though the pain may be controlled by sedation or anesthesia, the injection of these on the skin needs needle use. It is true that the probability of infection will increase with more skin punctures. In this paper, we develop

* Corresponding author, email: wooram.park@utdallas.edu

an insertion plan for a flexible needle reaching multiple targets from a single port with minimized tissue damage.

Constant improvements of medical procedures led to the appearance of a flexible needle with a bevel tip resulting in increased steerability and maneuverability within the soft tissue[31] compared with conventional stiff needles. In the past decade, this topic has received considerable attention in the literature due to its significant clinical potential. Percutaneous needle insertion is used in medical applications such as biopsies, regional anesthesia, neurosurgery, and brachytherapy.[4,27,32,34] The survey on the state-of-the-art and research trends in this area is presented in Abolhassani *et al.*[1] The substantial effort to gain good understanding of the nature of various aspects of needle motion and its interaction with the tissue was put forth in a number of experimental works.[8,12,15,17,19,22,24,25,29–31] In particular, several groups of authors[12,16,19,26,31] introduced a variety of needle steering methods and robotic devices facilitating these methods. For the force interaction between the flexible needle and the tissue, Misra *et al.*[17] studied the asymmetric force distribution on the needle tip, and Reed *et al.*[25] analyzed the effect of torsional friction on the accuracy of needle manipulation. The interaction force causes tissue deformation and thus affects needle placement accuracy. While clinical practitioners have addressed this issue based on their own experience, several research groups[3,7,8,13] developed models quantifying needle placement errors due to tissue deformation. In the clinical setting, needle insertion relies on medical imaging such as ultrasound, CT, and MRI, therefore many studies have focused on 2D motion planning.[2,3,24]

Currently, a number of 3D path planning algorithms for flexible steerable needles are available in the literature. In the works of Park *et al.*,[20,21] stochastic representation of the needle insertion process is used and solutions are generated by utilizing the stochastic differential equation and the corresponding Fokker–Planck equation. Numerical optimization of a cost function was used in Duindam *et al.*,[10] and path planning for "fireworks" needle insertion based on the Forest of Rapidly Exploring Random Trees in Xu *et al.*[33] were employed to solve for feasible 3D trajectories while avoiding obstacles.

A few motion planning approaches were based on geometric properties of a needle motion trajectory. In particular, Hauser *et al.*[13] used a closed-loop control policy executing helical paths, while two geometric approaches that generalized the Dubins car representation[9] for optimal path planning in the 3D space were developed in refs. [11, 14]. In both of these latter approaches, however, the start and goal points are connected by a series of circles of large curvature, which limits the practical realization of these approaches to flexible needles that generates high-curvature trajectory (e.g. prebent needles[26]).

As can be seen in the multiple images of the needle inserted in the phantom tissue such as in ref. [31], the curvature of the needle path is quite small. This is also confirmed by the parameter estimation study[22] where the trajectory curvature of the flexible needle was estimated at $\kappa = 0.0062\ \text{mm}^{-1}$, which is equivalent to the radius of curvature, $R = 161.3$ mm. In order to support this idea, we carried out an experiment described in the Appendix. We note that very complex needle trajectories with many frequent turns might be unfeasible for the practical insertion of the flexible needle because the needle depth does not exceed the size of the human body and the curvature of the needle trajectory is not large. As Fig. 1 provides the approximate comparison between the human liver and the needle curve sizes, the curvature of the needle trajectory is not high enough to generate the complex needle path with many turns. Furthermore, many turns of a needle can cause tissue damage and needle positioning errors. This observation justifies the very simple insertion strategy proposed in this paper. As aforementioned, for example, two targets are reached by a needle through insertion, partial retraction, turn, and reinsertion.

The majority of previous works dealt with finding feasible trajectories for reaching a single goal given a single insertion point (or port), while only a few focused on reaching multiple goals[14,33] and determining the insertion point.[2,23] Therefore, while the needle path planning in the 3D space for obstacle avoidance is well studied, not a large number of approaches allowing to reach multiple targets from a single port with minimum tissue damage have been reported.

In this paper, we make three key contributions. First, we present a new and simple geometric approach for a flexible needle reaching three target points in the 3D space. This plan uses the fact that multiple targets in tissue can be reached by a flexible needle through a series of insertion, partial retraction, turn, and new insertion. The cost function that measures the tissue damage is defined and then minimized with respect to the insertion point, the insertion direction, and the target order.

https://doi.org/10.1017/S0263574713001161 Published online by Cambridge University Press

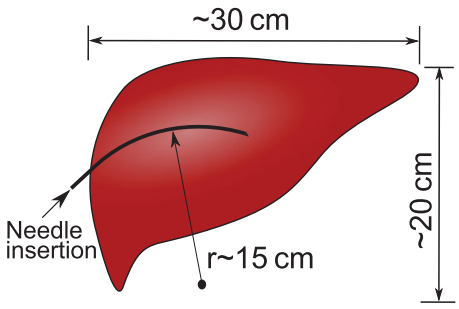

Fig. 1. (Colour online) Comparison of human liver and needle curve dimensions.

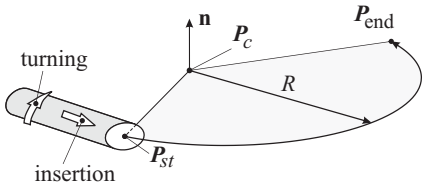

Fig. 2. Illustration of the bevel-tip needle. When simple insertion without turning is applied to the needle base, the needle travels along a planar arc.

Through the minimization, the lengths for intermediate insertion and retraction, and the angles of intermediate rotation (or turning) will also be obtained. Second, we present the reachability conditions that enhance the computational efficiency of the proposed approach. Third, we discuss the extensions of the algorithm to the case of more than three target points and the more complex cases of obstacle avoidance.

2. Assumptions, Notation, and Problem Statement

In this paper we use the unicycle model for the needle kinematics developed in ref. [31]. In other words, the needle is assumed to be following an arc of a perfect circle when it is inserted without the rotation (or turning) input. As emphasized in the conclusion section of ref. [31], this kinematic model is suitable when "tissue is relatively stiffer than the needle." In Fig. 2, the scheme of a bevel-tip needle and the associated geometry are presented. The radius of curvature R is determined by physical interaction between the flexible needle and the tissue. A method to estimate this parameter was introduced in Park *et al.*[22] In our work, we develop a needle insertion algorithm under a non-deformable and homogeneous environment. In addition, we assume that the first target is reached by the needle along a single arc from a single port. This is reasonable because the radius of curvature of the needle trajectory is large enough for practical use as illustrated in Fig. 1.

When the needle tip is assumed to be following a circular arc as stated above, its instantaneous coordinates can be described by parametric equations. Since the needle is assumed to be moving in an ideal environment, the insertion and turning velocities do not influence the feasible needle configuration that allows the needle to reach all the target points.[31] Therefore, all the needle paths are described by the primitives identified in the notation below, and the entire motion planning algorithm is based on the problem of *fitting circular arcs of a given radius through two points in the given plane*.

In this work we consider the number of ports and the tissue damage by forward insertion. The number of ports should be limited because many skin punctures (equivalently many ports) may cause pain and infection. Our approach is advantageous because it uses only one port. Even though the pain can be reduced by anesthesia, we use needle to inject anesthesia, which may again increase the possibility of infection. In addition, the tissue damage by the forward insertion of the needle should be minimized to reduce internal bleeding and help faster recovery. In this context, we assume

https://doi.org/10.1017/S0263574713001161 Published online by Cambridge University Press

that retraction does not produce significant tissue damage because during retraction, the needle tip will cause no tissue rupture and follow the already made channel by the prior forward insertion. Although the rotation (or turning) of the needle tip around the needle axis will damage the tissue, the rotation motion is not dominant in the proposed insertion plan. For three and four targets, only two and three rotations are engaged respectively. Compared with the damage by the forward insertion, the damage by the rotation is negligible, mainly because the number of rotations (or turns) is only $n-1$, where n is the number of targets. We will develop an approach generating the needle trajectory which causes minimized tissue damage while targeting multiple locations from a single port.

Next, we introduce the notation used throughout the paper. First, P_i, P_1, P_2, and P_3 denote the insertion and the first, second, and third target points, respectively. This notation remains the same even if the sequence in which the points are reached changes, in which case the coordinates of P_1, P_2, and P_3 are switched around. The notation $\mathbf{P}_k = [x_k, y_k, z_k]^{\mathrm{T}}$ stands for a vector of coordinates of a point P_k, and $\mathbf{P}_{ck}$ denotes the coordinates of the center of the circle leading to that point P_k. A normal vector of the plane in which this circle is located is denoted by $\mathbf{n}_k$. For brevity, the notation $arc(\mathbf{n}, \mathbf{P}_c, R, \mathbf{P}_{st}, \mathbf{P}_{\mathrm{end}})$ substitutes the following expression: the circular arc in the plane with the normal vector $\mathbf{n}$, center at $\mathbf{P}_c$, and radius R passes through points $\mathbf{P}_{st}$ and $\mathbf{P}_{\mathrm{end}}$ in the counterclockwise direction, as viewed from the tip of the vector $\mathbf{n}$. Note that if the starting and ending points are the same, the $arc(\mathbf{n}, \mathbf{P}_c, R, \mathbf{P}_{st}, \mathbf{P}_{\mathrm{end}})$ represents a closed circle.

The path planning algorithm presented in the next section describes a plan for finding the feasible 3D needle trajectories connecting the insertion point and three target points. This plan is executed by a sequence of insertions, partial retractions, turning, and new insertions toward subsequent target points. By varying the coordinates of the insertion point, the insertion direction, and the target sequence, we find optimal needle trajectory which produces the minimum tissue damage while reaching multiple targets.

3. Path Planning Algorithm

In this section, the path planning algorithm (Algorithm 1) is presented. In this algorithm, the general strategy for reaching three target points by insertion, partial retraction, turning a needle to a certain angle, and a new insertion toward the subsequent target point is communicated. Algorithm 2 that will be linked to Algorithm 1 describes the procedure of finding the turning point on the current needle trajectory for partial retraction and a new insertion toward the next target point.

3.1. Mathematical preliminaries: Circles in 3D space

The circle in the plane arbitrarily oriented in the 3D space can be represented by the following parametric equations:

$$\mathbf{P} = \mathbf{P}_c + \frac{R}{|\mathbf{u}|}\left(\mathbf{u}\cos t + \frac{1}{|\mathbf{n}|}(\mathbf{n}\times\mathbf{u})\sin t\right), \tag{1}$$

where

$\mathbf{P} = [P_x, P_y, P_z]^{\mathrm{T}}$ is the vector of coordinates of a point on the circle,
$\mathbf{P}_c = [x_c, y_c, z_c]^{\mathrm{T}}$ is the vector of coordinates of the center of the circle,
$\mathbf{n} = [n_x, n_y, n_z]^{\mathrm{T}}$ is a normal vector of the plane,
$\mathbf{u} = [n_y, -(n_x + n_z), n_y]^{\mathrm{T}}$ is a vector from the center toward the point on the circle in the plane.

For convenience, the vector Eq. (1) can be represented in the following componentwise form:

$$\begin{aligned} P_x &= x_c + R(A_x\cos t + B_x\sin t),\\ P_y &= y_c + R(A_y\cos t + B_y\sin t),\\ P_z &= z_c + R(A_z\cos t + B_z\sin t), \end{aligned} \tag{2}$$

https://doi.org/10.1017/S0263574713001161 Published online by Cambridge University Press

where

$$
\begin{aligned}
A_x &= A_z = n_y/|\mathbf{u}|, \qquad B_x = \left(n_y^2 + n_x n_z + n_z^2\right)/(|\mathbf{u}||\mathbf{n}|),\\
A_y &= -(n_x + n_z)/|\mathbf{u}|, \qquad B_y = n_y(n_z - n_x)/(|\mathbf{u}||\mathbf{n}|),\\
B_z &= \left(-n_x^2 - n_x n_z - n_y^2\right)/(|\mathbf{u}||\mathbf{n}|),\\
|\mathbf{u}| &= \sqrt{2n_y^2 + (n_x + n_z)^2}, \qquad |\mathbf{n}| = \sqrt{n_x^2 + n_y^2 + n_z^2}.
\end{aligned} \tag{3}
$$

The inverse problem of finding the parameter t^* corresponding to the given vectors $\mathbf{P}$, $\mathbf{P}_c$, $\mathbf{u}$, and $\mathbf{n}$ can be solved as follows:

$$
\begin{aligned}
\sin t^* &= \frac{(P_y - y_c)(A_x + A_z) - A_y(P_x - x_c + P_z - z_c)}{R(B_y(A_x + A_z) - A_y(B_x + B_z))},\\
\cos t^* &= \frac{(P_x - x_c + P_z - z_c)}{R(A_x + A_z)} - \frac{B_x + B_z}{A_x + A_z}\sin t^*,\\
t^* &= \operatorname{atan2}(\sin t^*, \cos t^*).
\end{aligned} \tag{4}
$$

This inverse problem is used in Algorithm 2.

3.2. Algorithm 1

General strategy:

1. Select the sequence in which the target points are reached.
2. Select the insertion point.
3. In the plane passing through points P_i, P_1, and P_2, draw the right-arc passing through points P_i and P_1.
4. Generate a family of arcs passing through points P_i and P_1 by rotating the arc from stage 3 about the axis $P_i P_1$.
5. For each sampled arc from stage 4, numerically find the root of the function defined by Algorithm 2. If it exists, this is the first turning point P_{turn1} and go to stage 6. Otherwise, return failure.
6. Calculate the first turning angle as

$$
\theta_{t1} = \operatorname{acos}\frac{(\mathbf{P}_{c1} - \mathbf{P}_{\text{turn1}}, \mathbf{P}_{c2} - \mathbf{P}_{\text{turn1}})}{\|\mathbf{P}_{c1} - \mathbf{P}_{\text{turn1}}\| \cdot \|\mathbf{P}_{c2} - \mathbf{P}_{\text{turn1}}\|}. \tag{5}
$$

7. Generate the needle path from the point P_{turn1} found in stage 5 to P_2.
8. Search for the second turning point P_{turn2} on the arc $\widehat{P_{\text{turn1}}P_2}$ from stage 7 using Algorithm 2. If it is found, go to stage 9. Otherwise, go to stage 11.
9. Calculate the second turning angle as

$$
\theta_{t2} = \operatorname{acos}\frac{(\mathbf{P}_{c2} - \mathbf{P}_{\text{turn2}}, \mathbf{P}_{c3} - \mathbf{P}_{\text{turn2}})}{\|\mathbf{P}_{c2} - \mathbf{P}_{\text{turn2}}\| \cdot \|\mathbf{P}_{c3} - \mathbf{P}_{\text{turn2}}\|}. \tag{6}
$$

10. Generate the needle path from P_{turn2} to P_3.
11. Repeat stages 5—10 for each arc from stage 4.
12. Select the combination of paths $\widehat{P_i P_1}$, $\widehat{P_{\text{turn1}}P_2}$, and $\widehat{P_{\text{turn2}}P_3}$ for which the sum of arc lengths given by

$$
l = R\,(\theta_1 + \theta_2 + \theta_3) \tag{7}
$$

https://doi.org/10.1017/S0263574713001161 Published online by Cambridge University Press

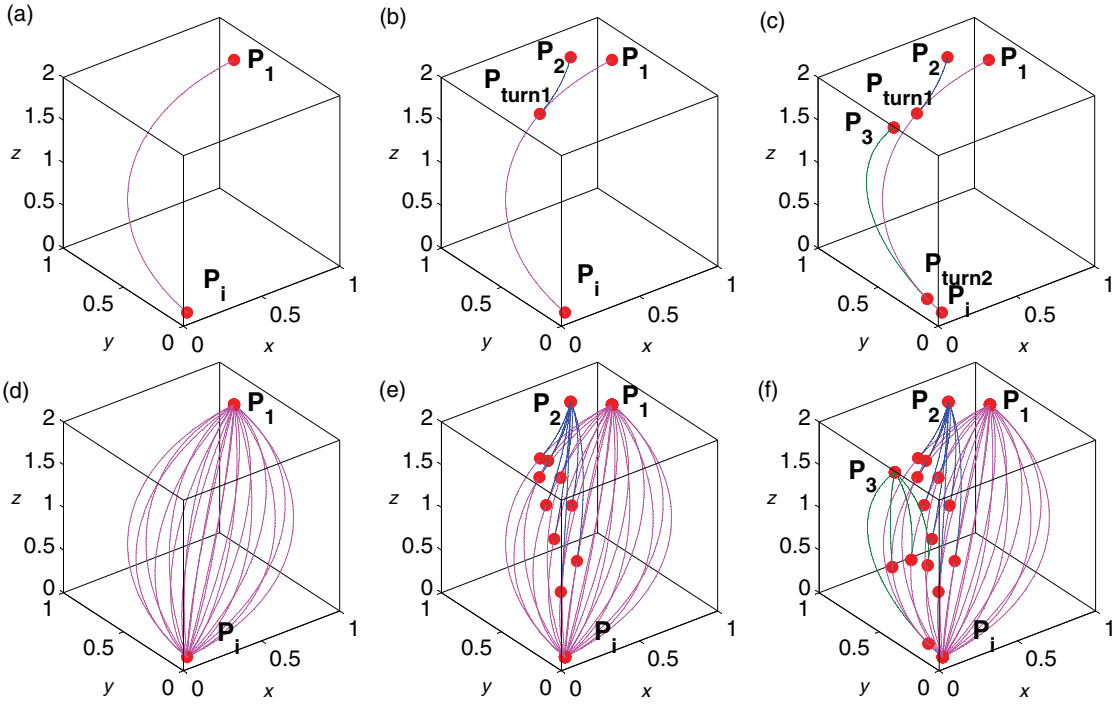

Fig. 3. (Colour online) Illustration of the algorithm for generating the optimal needle insertion trajectory for a selected target sequence and a selected insertion location. Each arc trajectory is obtained by connecting (a) P_i and P_1, (b) P_i, P_1, and P_2, and (c) P_i, P_1, P_2, and P_3. The respective families of trajectories (d,e,f) are generated by rotating the configuration in (a) about the axis $P_i P_1$ and finding the turning points for arcs leading to P_2 and subsequently P_3.

is minimal, where

$$\theta_1 = \mathtt{acos}\frac{(\mathbf{P}_i - \mathbf{P}_{c1}, \mathbf{P}_1 - \mathbf{P}_{c1})}{\|\mathbf{P}_i - \mathbf{P}_{c1}\| \cdot \|\mathbf{P}_1 - \mathbf{P}_{c1}\|}, \tag{8}$$

$$\theta_2 = \mathtt{acos}\frac{(\mathbf{P}_{\mathrm{turn1}} - \mathbf{P}_{c2}, \mathbf{P}_2 - \mathbf{P}_{c2})}{\|\mathbf{P}_{\mathrm{turn1}} - \mathbf{P}_{c2}\| \cdot \|\mathbf{P}_2 - \mathbf{P}_{c2}\|}, \tag{9}$$

$$\theta_3 = \mathtt{acos}\frac{(\mathbf{P}_{\mathrm{turn2}} - \mathbf{P}_{c3}, \mathbf{P}_3 - \mathbf{P}_{c3})}{\|\mathbf{P}_{\mathrm{turn2}} - \mathbf{P}_{c3}\| \cdot \|\mathbf{P}_3 - \mathbf{P}_{c3}\|}. \tag{10}$$

This is the optimal needle trajectory for the selected insertion point and the sequence of target points.

13. For different sequences of target points and insertion point, repeat stages 3 through 12.

The illustration of stages 3–12 of Algorithm 1 is presented in Fig. 3, while the optimal needle path configuration identified in stage 12 is shown in Fig. 4.

3.3. Algorithm 2

Finding the turning point:

In order to find the location of the turning point at the arc connecting points P_i and P_1, the root (or the minimum norm solution) of the following algorithmically described vector function is found numerically. It can be shown that the coordinates of a turning point satisfy a system of nonlinear algebraic equations. Due to the high complexity of this system, an algorithmic description is preferred. In what follows, let us assume we have an $arc(\mathbf{n}_1, \mathbf{P}_{c1}, R, \mathbf{P}_1, \mathbf{P}_i)$. Note the reversed order of the starting and ending points which results from the convention of first generating the right-arc from point P_i to P_1. We are looking for a point with coordinates $\mathbf{P}_{\mathrm{turn1}} = [x_{\mathrm{turn1}},\ y_{\mathrm{turn1}},\ z_{\mathrm{turn1}}]^{\mathrm{T}}$ which lies on that arc

https://doi.org/10.1017/S0263574713001161 Published online by Cambridge University Press

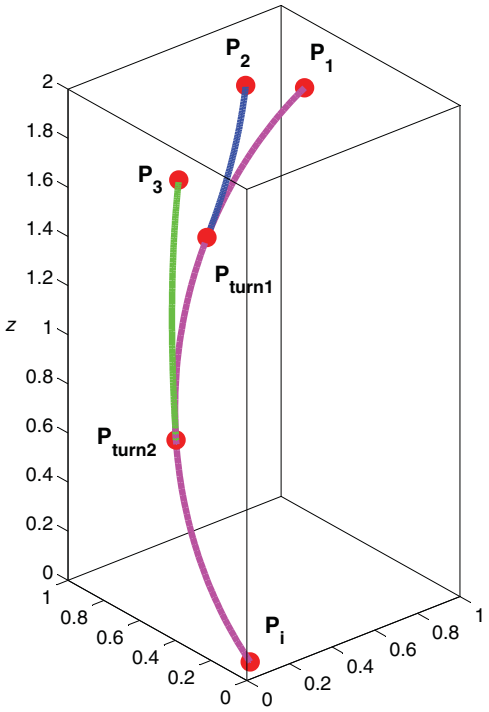

Fig. 4. (Colour online) Needle path configuration corresponding to the minimum sum of arc lengths (7) in the family of trajectories in Fig. 3(f).

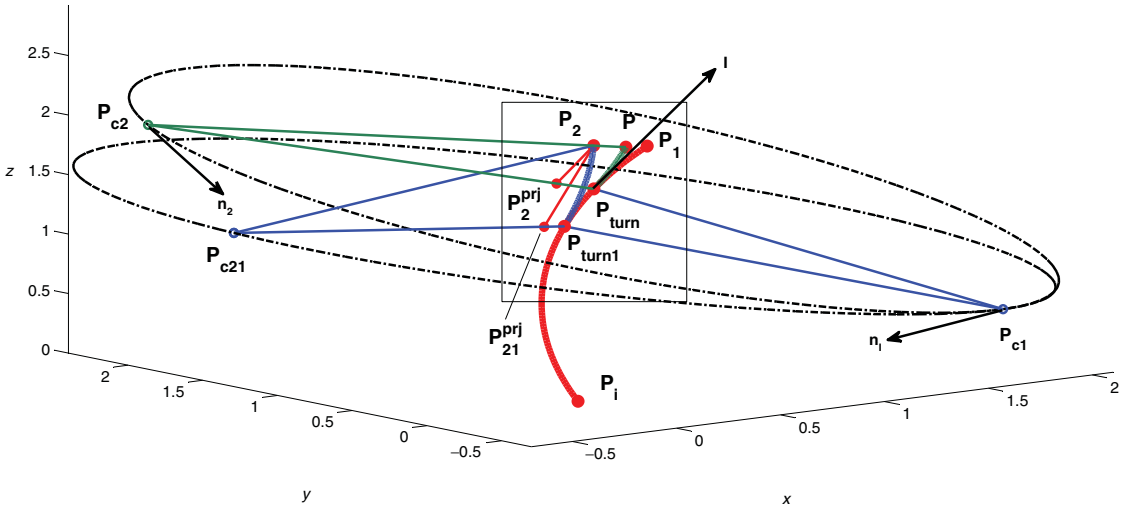

Fig. 5. (Colour online) Illustration of finding the turning point using Algorithm 2. The area within the rectangle is magnified in Fig. 6. Black circles represent the locus of points P_{c2} and P_{c21}.

such that if we turn the needle at this point, its further insertion will result in an $arc(\mathbf{n}_2, \mathbf{P}_{c2}, R, \mathbf{P}_{\text{turn1}}, \mathbf{P}_2)$ leading to the point $\mathbf{P}_2$. Figure 5 illustrates the algorithm given below that describes the vector function whose root is being sought. In this figure, along with the final configuration with the point $\mathbf{P}_{\text{turn1}}$ found, the point $\mathbf{P}_{\text{turn}}$ which the algorithm uses at the current iteration is shown for illustrative purposes. Therefore, all the stages of the algorithm will be formulated for the point $\mathbf{P}_{\text{turn}}$. For completeness, all the points in Figs. 5 and 6 corresponding to the final needle configuration have an additional subscript "1."

https://doi.org/10.1017/S0263574713001161 Published online by Cambridge University Press

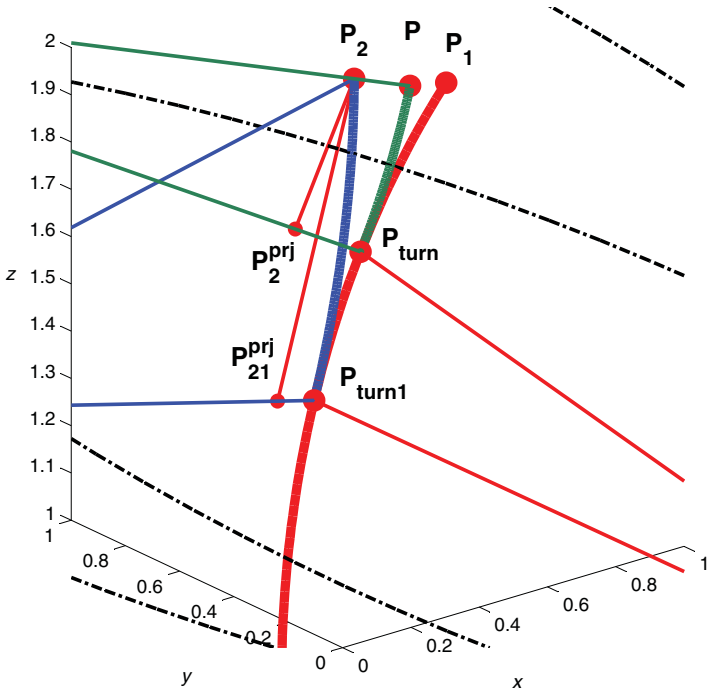

Fig. 6. (Colour online) The magnified area shown within a rectangle in Fig. 5.

1. Assume the coordinates $\mathbf{P}_{\text{turn}}$ are known.
2. Find the directional vector $\mathbf{l} = (\mathbf{P}_{\text{turn}} - \mathbf{P}_{c1}) \times \mathbf{n}_1$ of the tangent to the $arc(\mathbf{n}_1, \mathbf{P}_{c1}, R, \mathbf{P}_1, \mathbf{P}_i)$ at the point $\mathbf{P}_{\text{turn}}$.
3. Define the circle as an $arc(\mathbf{l}, \mathbf{P}_{\text{turn}}, R, \mathbf{P}_{c1}, \mathbf{P}_{c1})$.
4. Find the point $\mathbf{P}_2^{\text{prj}}$ as the projection of the point $\mathbf{P}_2$ onto the plane with the normal vector $\mathbf{l}$ passing through the point $\mathbf{P}_{\text{turn}}$.
5. Find the center $\mathbf{P}_{c2}$ of the $arc(\mathbf{n}_2, \mathbf{P}_{c2}, R, \mathbf{P}_{\text{turn}}, \mathbf{P}_2)$ as an intersection of the line with the directional vector $\mathbf{P}_2^{\text{prj}} - \mathbf{P}_{\text{turn}}$ with the circle from stage 3.
6. Find the normal vector $\mathbf{n}_2 = \mathbf{l} \times (\mathbf{P}_{c2} - \mathbf{P}_{\text{turn}})$.
7. Assuming $\mathbf{n} = \mathbf{n}_2$, $\mathbf{P} = \mathbf{P}_2$, and $\mathbf{P}_c = \mathbf{P}_{c2}$, find the corresponding t^* from Eqs. (3) and (4).
8. Evaluate Eqs. (2) at the value of parameter t^* found from stage 7. This results in coordinates $\mathbf{P}$ as a function of coordinates $\mathbf{P}_{\text{turn}}$.
9. The vector function whose root is being found comprises the following expressions:

$$\mathbf{F}_1(\mathbf{P}_{\text{turn}}) = (x_{\text{turn}} - x_{c1})^2 + (y_{\text{turn}} - y_{c1})^2 + (z_{\text{turn}} - z_{c1})^2 - R^2, \tag{11}$$

$$\mathbf{F}_2(\mathbf{P}_{\text{turn}}) = \mathbf{n}_1 \cdot (\mathbf{P}_{\text{turn}} - \mathbf{P}_{c1}), \tag{12}$$

$$\mathbf{F}_3(\mathbf{P}_{\text{turn}}) = (P_x - x_2)^2 + (P_y - y_2)^2 + (P_z - z_2)^2. \tag{13}$$

Expressions (11)–(13) equated to zero imply that the point $\mathbf{P}_{\text{turn}}$ must – directly as in Eqs. (11) and (12) or indirectly as in Eq. (13) – satisfy the following conditions: (a) $\mathbf{P}_{\text{turn}}$ lies on the $arc(\mathbf{n}_1, \mathbf{P}_{c1}, R, \mathbf{P}_1, \mathbf{P}_i)$, (b) $\mathbf{P}_{\text{turn}}$ lies in the plane with the normal vector $\mathbf{n}_1$ passing through the point $\mathbf{P}_{c1}$, and (c) coordinates of points $\mathbf{P}$ and $\mathbf{P}_2$ should match.[1]

[1] To implement Algorithm 2, we used the numerical solver *fsolve* in Matlab.

https://doi.org/10.1017/S0263574713001161 Published online by Cambridge University Press

4. Reachability

4.1. Mathematical preliminaries: tori and planes in 3D space

In this section, equations of a torus and a plane in 3D space are reviewed, because these 3D objects will be used to define the reachability conditions in the next section.

A torus in the 3D space radially symmetric about the z-axis can be described by the following equation:

$$f(x, y, z) = \left(R_{mj} - \sqrt{x^2 + y^2}\right)^2 + z^2 - R_{mn}^2 = 0, \tag{14}$$

where R_{mj} and R_{mn} are the major and minor radii, respectively. We need, however, the equation of a torus arbitrarily oriented in the 3D space. We consider the plane with the normal vector $\mathbf{n}$ passing through the point $\mathbf{P}_c$ and assume that the torus possesses radial symmetry about the line with the directional vector $\mathbf{n}$ and axial symmetry about the plane given by the normal vector $\mathbf{n}$. As a result, the equation of a rotated torus with the center $\mathbf{P}_c$ can be obtained by combining Eq. (14) with the following coordinate transformation:

$$[x, y, z]^{\mathrm{T}} = \mathbf{A}[x', y', z']^{\mathrm{T}} + \mathbf{P}_c, \tag{15}$$

where

$$\mathbf{A} = \left[\frac{\mathbf{u}}{|\mathbf{u}|} \quad \frac{1}{|\mathbf{n}||\mathbf{u}|}(\mathbf{n} \times \mathbf{u}) \quad \frac{\mathbf{n}}{|\mathbf{n}|}\right] \tag{16}$$

is the matrix of basis transformation and $\mathbf{u}$ is a part of Eq . (1). If we need to check whether the point with coordinates (x, y, z) lies inside, on, or outside the torus, the function in Eq. (14) should be computed for $[x', y', z']$ in Eq. (15), and the sign of $f(x', y', z')$ yields one of the following outcomes:

$$\begin{aligned} f(x', y', z') &< 0 \quad \text{inside the torus,} \\ f(x', y', z') &= 0 \quad \text{on the torus,} \\ f(x', y', z') &> 0 \quad \text{outside the torus.} \end{aligned} \tag{17}$$

In addition, the plane with the normal vector $\mathbf{l}$ passing through the point $\mathbf{P}_c$ in the 3D space is given by the equation

$$p(x, y, z) = \mathbf{l} \cdot ([x, y, z]^{\mathrm{T}} - \mathbf{P}_c) = 0. \tag{18}$$

The conditions determining whether a point with coordinates (x, y, z) lies in the half-spaces toward the positive or negative directions of the normal vector are given as

$$p(x, y, z) > 0, \tag{19}$$

$$p(x, y, z) < 0, \tag{20}$$

respectively.

4.2. Reachable sets

The reachability conditions for steerable needles were studied in a number of publications.[11,20] The term *reachability* implies a set of points (or needle poses) that a needle can reach for given location and direction of insertion. In this paper, we use the reachability condition to reduce computational time at every insertion point. It can be seen in Fig. 3(e) that the orientation of some sample trajectories connecting points P_i and P_1 does not allow for the turning point P_{turn1} to be found by implementing Algorithm 2 because the subsequent insertion from the turning point does not reach P_2. When this is the case, it may take a numerical solver a longer time to arrive at no solution than the time it actually arrive at one. Therefore, having the family of trajectories $\widehat{P_{\text{turn1}} P_2}$ shown in Fig. 3(e), we are looking for the conditions that these trajectories satisfy in order to rule out unfeasible trajectories.

https://doi.org/10.1017/S0263574713001161 Published online by Cambridge University Press

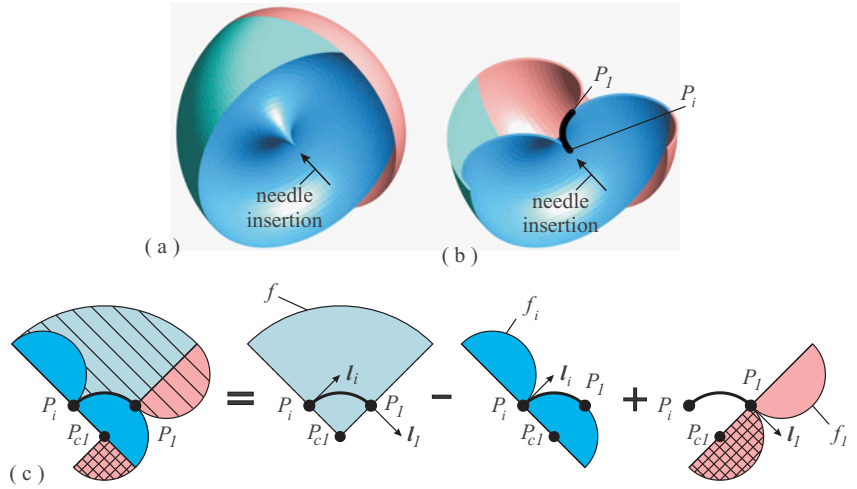

Fig. 7. (Colour online) Illustration of reachability conditions: (a) The set of points reachable when the needle trajectory connecting the insertion point P_i and the first target point P_1 is known, (b) its cutaway view, and (c) decomposition of the solid in (a) for the derivation of reachability conditions.

Identification of these conditions can be done by visualizing the possible needle trajectories emanating from the needle path to the current target point toward the subsequent target and describing the resulting set mathematically. First, we generate an arc $\widehat{P_i P_1}$ in the plane with the normal vector $\mathbf{n}_1$. Next, we revolve two semicircles of radius R lying in the plane with normal vector $\mathbf{n}_1$ tangent to the arc $\widehat{P_i P_1}$ at the points P_i and P_1 about the lines tangent to the same arc defined by directional vectors $\mathbf{l}_i$ and $\mathbf{l}_1$, respectively. The family of toroidal surfaces between those at points P_i and P_1 represents the set of possible needle trajectories from the point P_{turn1} to the point P_2. In other words, this set can be visualized as a solid enclosed within the three surfaces: a *concave* half of a horn torus at the point P_i radially symmetric about the line $\mathbf{l}_i$, a *convex* half of a horn torus at the point P_1 radially symmetric about the line $\mathbf{l}_1$, both with $R_{mj} = R_{mn} = R$, and a spindle torus at the point P_{c1} radially symmetric about the line $\mathbf{n}_1$ with $R_{mj} = R$ and $R_{mn} = 2R$, where R_{mj} and R_{mn} along with the equation of a torus are the major and minor radii as defined above. This solid and its cutaway view are shown in Figs. 7(a) and (b). A similar representation of the reachable set for a flexible needle is presented in Hauser *et al.*[13] It is obvious that the point with coordinates (x, y, z) is reachable if it lies on one of the surfaces in Figs. 7(a) and (b) or within the solid as defined above. However, due to the high geometric complexity of this solid, in order to derive reachability conditions, we need to decompose this solid into an intersection of simpler ones. The section of such a decomposition with the plane with normal vector $\mathbf{n}_1$ passing through the point $\mathbf{P}_{c1}$ along with everything visible beyond this plane is shown in Fig. 7(c). Note that while the hatched area illustrates the section of the reachable set, the cross-hatched area is the section of the segment of a toroidal surface that is also reachable, and it is not a part of the solid.

Reachability conditions are shown in the flowchart in Fig. 8. In these conditions, $f(x', y', z')$, $f_i(x', y', z')$, and $f_1(x', y', z')$ represent the torus function in Eq. (14) with the coordinate change (15) for the spindle torus and two horn tori at points P_{c1}, P_i, and P_1 with axes of radial symmetry defined by vectors $\mathbf{n}_1$, $\mathbf{l}_i$, and $\mathbf{l}_1$, respectively. Note that even though the coordinates (x', y', z') are the same for the above three functions, single primes are used solely for brevity, while for each function the local basis is different and oriented so that the local z-axis coincides with the axis of radial symmetry of the corresponding torus. At the same time, $p_i(x, y, z)$ and $p_1(x, y, z)$ denote the plane function in Eq. (18) with the normal vectors $\mathbf{l}_i$ and $\mathbf{l}_1$, respectively.

5. Examples and Discussion

5.1. Insertion without obstacles

In this section we apply the proposed insertion plan to a set of three targets without obstacles. For convenient demonstration, we use target points with dimensionless coordinates. Besides, the radius of

https://doi.org/10.1017/S0263574713001161 Published online by Cambridge University Press

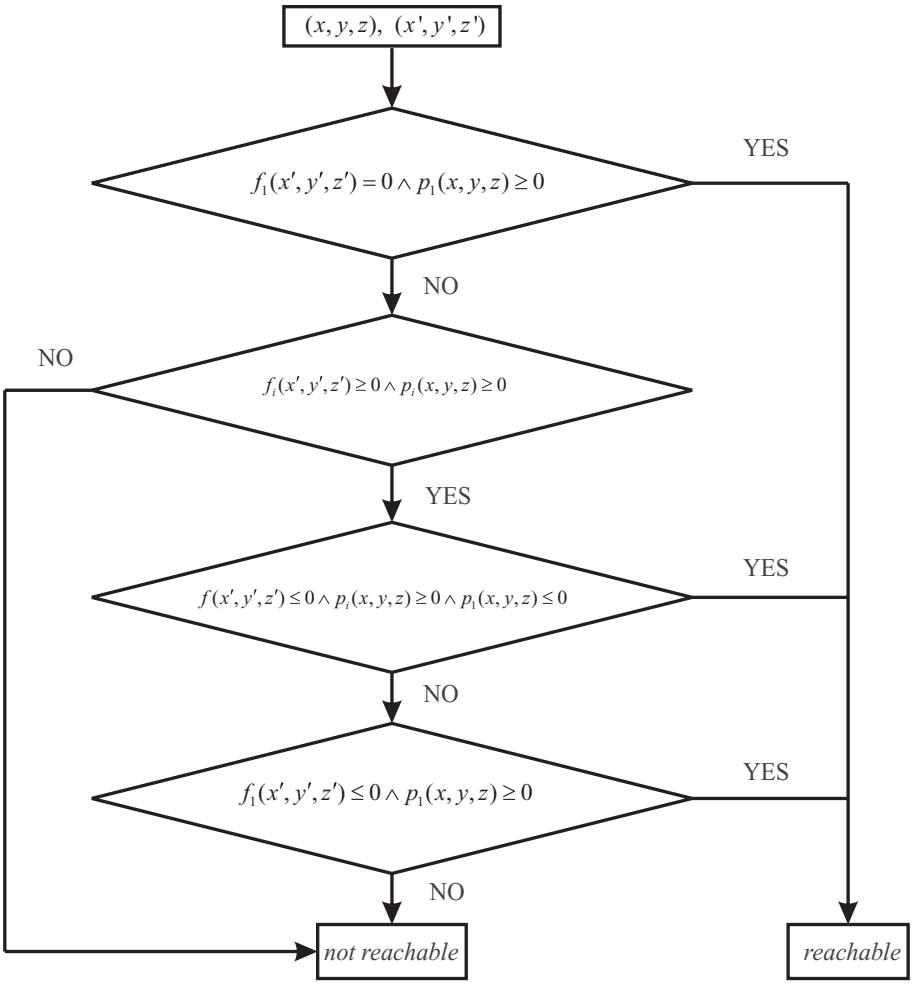

Fig. 8. The flowchart illustrating the conditions defining the reachable set shown in Fig. 7. The notation $\wedge$ stands for the logical AND.

curvature of the needle trajectory R is defined by a dimensionless length. To convert these coordinates and length to ones with actual dimension unit, we can multiply them by the ratio R'/R, where R' is the dimensional radius of curvature of the needle trajectory determined experimentally. The radius R is a fixed value during optimization. In addition, we consider a cuboid between the two vertices (0, 0, 0) and (1, 1, 2) which is the medium where the target points are located. Finally, we assume that the insertion point lies in the xy-plane in the domain $[x_{\min}, x_{\max}, y_{\min}, y_{\max}] = [0, 1, 0, 1]$.

Consider the target points in the 3D space given in Table I (Example 1). In what follows, the result for the selected example is obtained by the following process. First, we select the resolution of the search domain for the insertion point and the number of arcs in the family of trajectories generated in stage 4 of Algorithm 1 shown in Fig. 3(d). Second, for each order of target points, we generate the optimal needle configuration at every insertion point on the search domain grid. Third, for each of these optimal needle configurations, we compute the total length of trajectory, which represents the tissue damage, defined by Eq. (7). Fourth, we generate the tissue damage matrix **D** using the tissue damage estimation over the search domain grid. Each component of matrix **D** is the amount of tissue damage that would be caused if the needle was inserted from the corresponding port location. Fifth, for each insertion point on the search domain grid, we select the target point order corresponding to the minimum tissue damage. Finally, we plot the minimum tissue damage map for which we also determine the local minimum that corresponds to the optimal insertion point in the selected domain.

For Example 1, we choose the dimensionless radius of curvature of the needle trajectory $R = 1.5$, the resolution of 41×41 points for the insertion point search, $N_{12} = 271$ needle trajectories in the family from stage 4 of Algorithm 1, and the target point coordinates as $P_1(0.3, 0.65, 1.5)$,

https://doi.org/10.1017/S0263574713001161 Published online by Cambridge University Press

Table I. Parameters associated with the insertion procedure at the optimal insertion points for Examples 1 and 2.

Parameter	Example 1	Example 2
Target point coordinates	$P_1(0.3, 0.65, 1.5)$ $P_2(0.4, 0.3, 1.4)$ $P_3(0.1, 0.5, 1.6)$	$P_1(0.3, 0.65, 1.5)$ $P_2(0.4, 0.3, 1.4)$ $P_3(0.1, 0.5, 1.6)$
Obstacle location	None	(0.25, 0.25, 0.25)
Obstacle radius	None	0.15
Optimal target sequence	2-1-3	2-1-3
Optimal insertion point	(0.55, 0.45)	(0.625, 0.5)
Insertion direction	(–0.38, 0.28, 0.88)	(–0.42, 0.26, 0.87)
Traveling distance for insertion 1	1.4747	1.4929
Traveling distance for retraction 1	0.73842	0.74255
Turning angle 1	137.02°	139.28°
Traveling distance for insertion 2	0.82211	0.81598
Traveling distance for retraction 2	0.6169	0.59378
Turning angle 2	104.51°	106.96°
Traveling distance for insertion 3	0.74355	0.73417
Total tissue damage	3.0403	3.0431

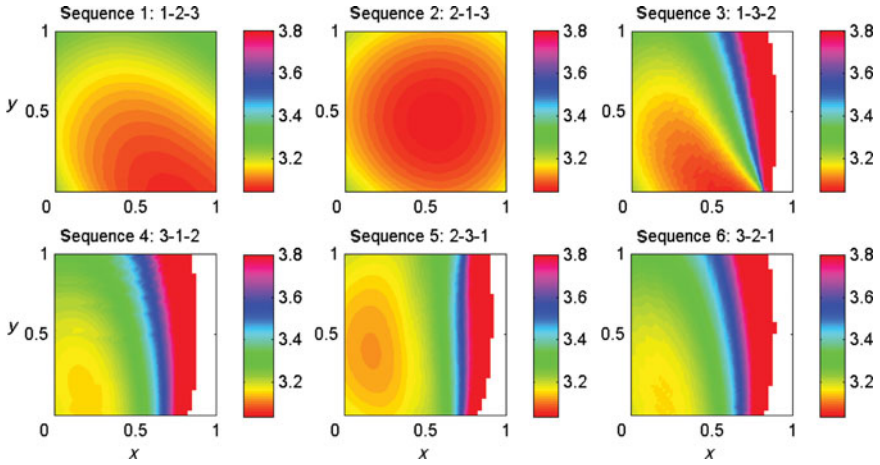

Fig. 9. (Colour online) The tissue damage maps for each order of target points calculated for Example 1. The scale bar shows the amount of total tissue damage.

$P_2(0.4, 0.3, 1.4)$, and $P_3(0.1, 0.5, 1.6)$. As aforementioned, the dimensionless length and location are used for more straightforward demonstration. The value 1.5 for the dimensionless radius was chosen by comparing the radius size and the target locations so that the setup can simulate realistic situations such as in Fig. 1. The tissue damage maps for each order of target points are shown in Fig. 9. The map of tissue damage shown in Fig. 10(a) over the insertion domain can be obtained by combining the six maps in Fig. 9. In other words, the tissue damage corresponding to an insertion location in Fig. 10(a) is obtained by selecting the minimum of six damage values corresponding to the insertion location in Fig. 9. We find the optimal insertion location denoted by the × mark in Fig. 10(a). The optimal order of target points is the targeting order with which we can get the minimum tissue damage. The needle configuration for the optimal insertion point and the optimal target order is shown in Fig. 10(b). The detailed list of parameters associated with the insertion is given in the column named Example 1 in Table I.

Figure 11 shows the benefit of our approach. In Fig. 11, the three targets of Example 1 are reached by three independent insertions. Each insertion is obtained such that each length of the needle trajectory is minimized. In Fig. 11(a), a flexible needle is inserted independently for the

https://doi.org/10.1017/S0263574713001161 Published online by Cambridge University Press

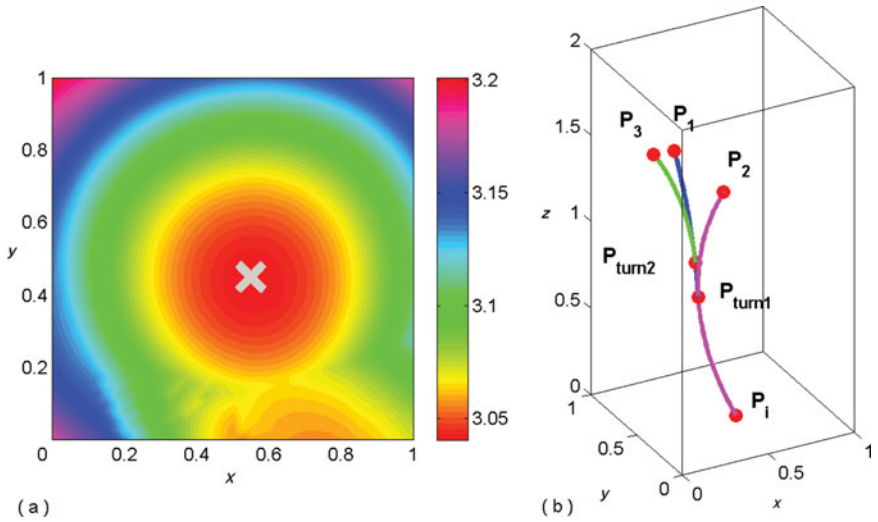

Fig. 10. (Colour online) (a) The minimum tissue damage map. Cross × indicates the optimal insertion point location. (b) Needle configuration for the optimal insertion point indicated in (a).

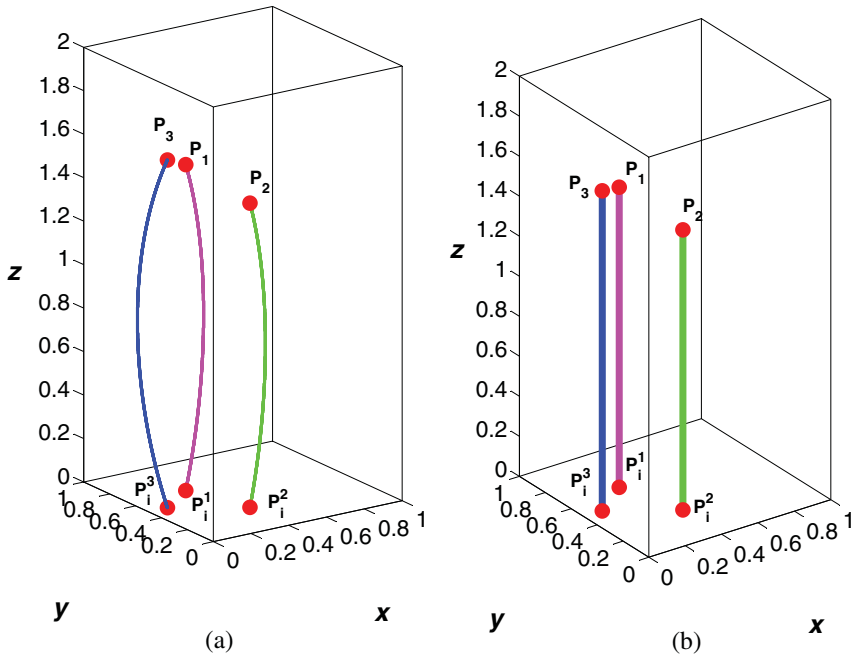

Fig. 11. (Colour online) Needle insertion for three targets with three independent new insertions. Each insertion is computed for minimum tissue damage. (a) Insertions of a flexible needle. (b) Insertions of a straight needle.

three targets. In Fig. 11(b), a straight needle is inserted independently for the three targets. For both demonstrations in Fig. 11, the target points are denoted by $\mathbf{P}_1$, $\mathbf{P}_2$, and $\mathbf{P}_3$, and the optimal insertion points are denoted by $\mathbf{P}_i^1$, $\mathbf{P}_i^2$, and $\mathbf{P}_i^3$. It is obvious that the total length of the needle trajectory from our approach (Fig. 10(b)) is much shorter than the results from Fig. 11. Specifically, the length of the needle trajectory from our approach is 3.0403 for Example 1 (see Table I), while the lengths of the trajectories are 4.72 for a flexible needle (Fig. 11(a)) and 4.5 for a straight needle (Fig. 11(b)). This means that our approach causes less tissue damage and less skin punctures than the multiple new insertions.

https://doi.org/10.1017/S0263574713001161 Published online by Cambridge University Press

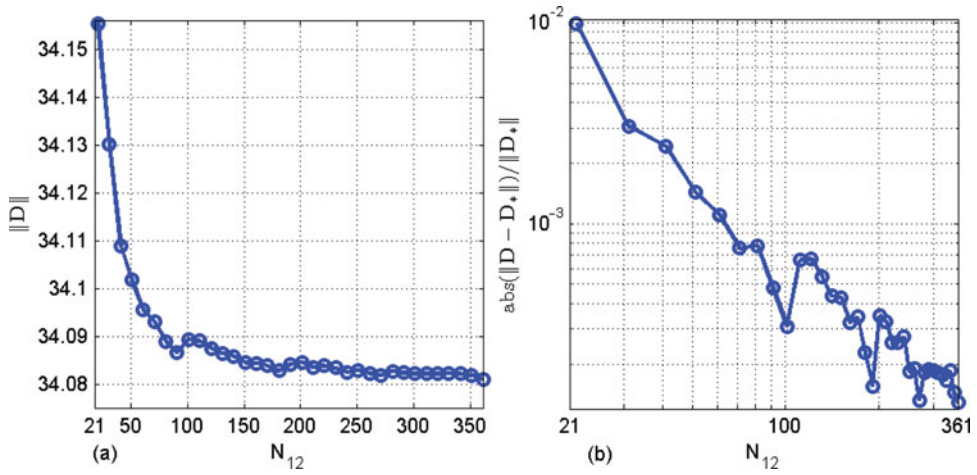

Fig. 12. (Colour online) (a) Norm $\|\mathbf{D}\|$, and (b) the error defined in Eq. (21) plotted versus N_{12} (the number of needle trajectories in the family from stage 4 of Algorithm 1).

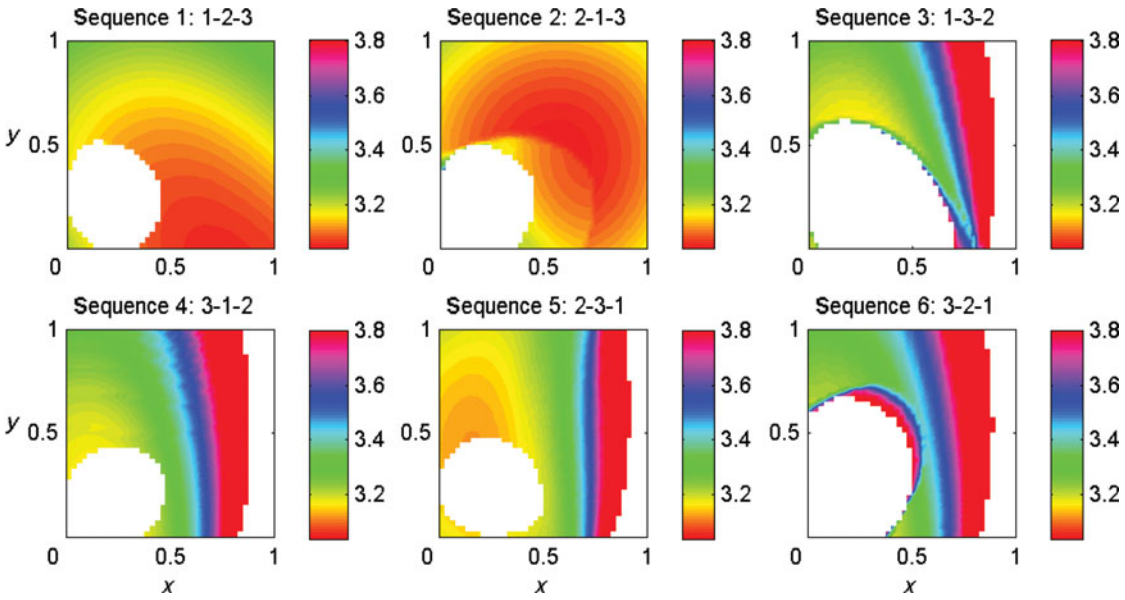

Fig. 13. (Colour online) The tissue damage maps for each order of target points calculated for Example 2. The spherical obstacle of radius $R_0 = 0.15$ is placed at the point (0.25, 0.25, 0.25). The gaps in the lower left corner correspond to the insertion points for which no feasible needle trajectories can be found.

It is also perceptive to carry out a convergence test to confirm the intuition that the minimum tissue damage map converges as the value of N_{12} increases. Note that N_{12} denotes the number of arcs in the family of trajectories generated in stage 4 of Algorithm 1. For this purpose, we select the resolution of 11×11 for the search domain grid and generate the damage map (which is represented by an 11×11 matrix) for different values of N_{12} from 21 to 361 with increments of 10. For the matrix of tissue damage denoted by $\mathbf{D}$, the error characterizing this matrix is written as

$$\text{error} = \frac{\|\mathbf{D} - \mathbf{D}_*\|}{\|\mathbf{D}_*\|}, \tag{21}$$

where $\|\cdot\|$ is the Euclidean norm of a matrix and $\mathbf{D}_*$ is the tissue damage map for $N_{12} = 361$. Norm $\|\mathbf{D}\|$ and the error defined by Eq. (21) are plotted versus N_{12} in Figs. 12(a) and (b), respectively.

https://doi.org/10.1017/S0263574713001161 Published online by Cambridge University Press

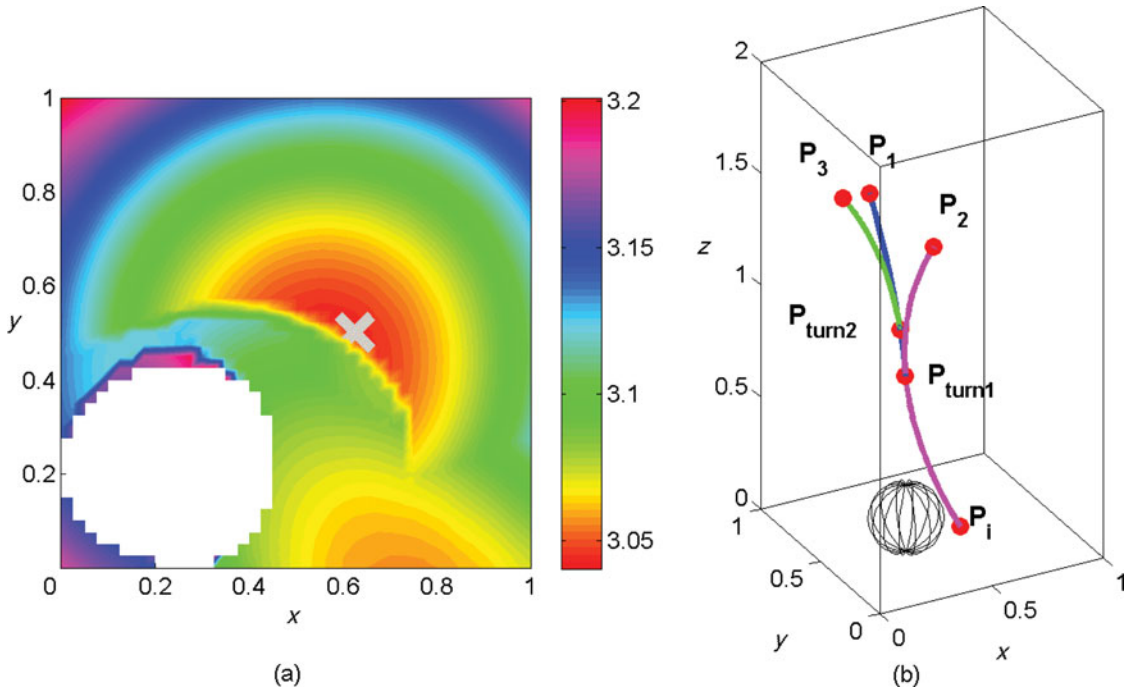

Fig. 14. (Colour online) (a) The minimum tissue damage map for Example 2. Cross **x** indicates the optimal insertion point location. (b) The needle configuration for the optimal insertion point indicated in (a).

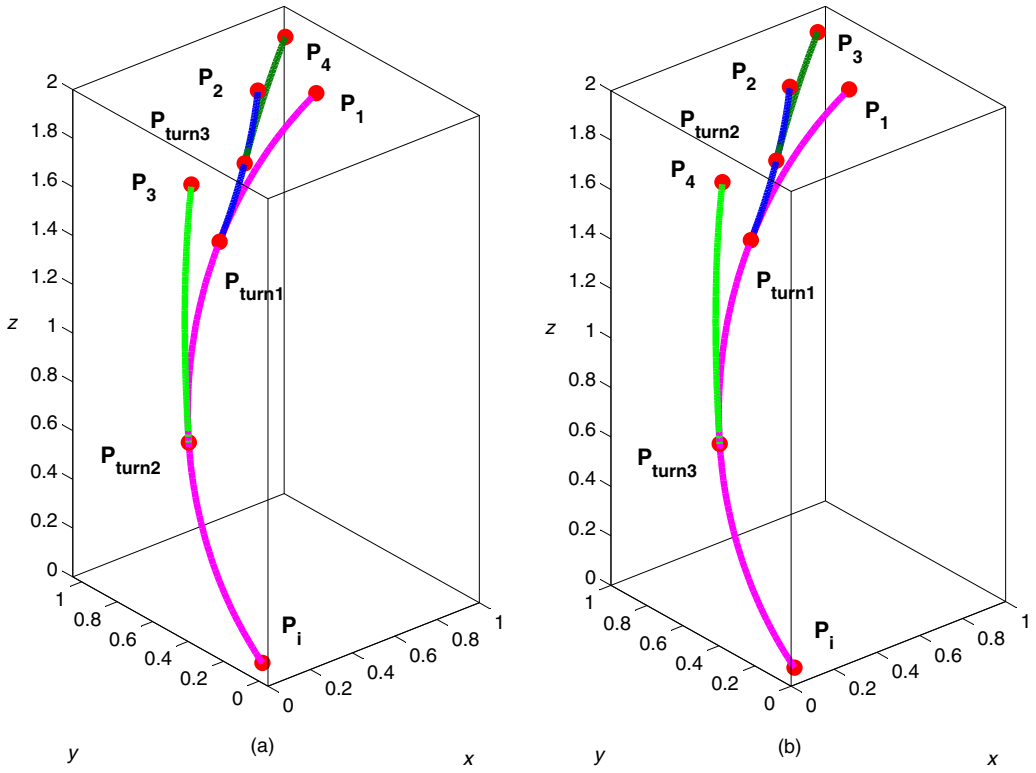

Fig. 15. (Colour online) An example of applying the path planning algorithm to the case of more than three target points is shown. In (a) the numbering of target points represents the initially selected sequence. Once the turning points P_{turn2} and P_{turn3} are found on arcs $\widehat{P_i P_1}$ and $\widehat{P_{\text{turn1}} P_2}$, the order of target points P_3 and P_4 needs to be changed as shown in (b).

https://doi.org/10.1017/S0263574713001161 Published online by Cambridge University Press

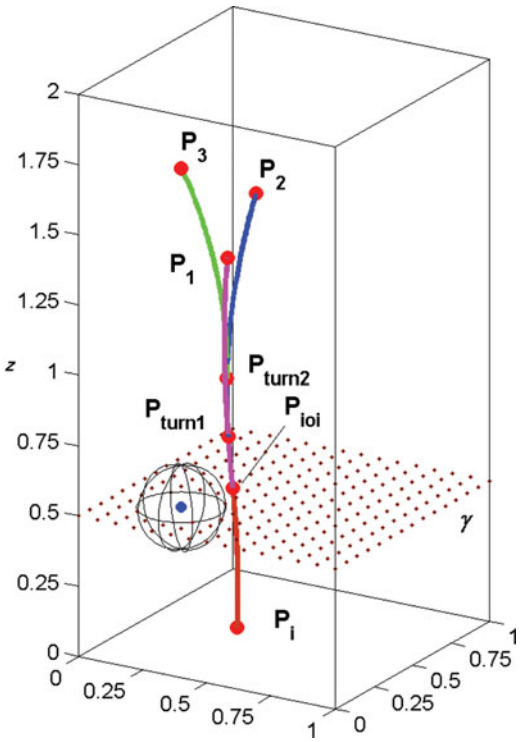

Fig. 16. (Colour online) Illustration of algorithm extension to the case of maneuvering around spherical obstacles.

5.2. Obstacle avoidance

The plan for reaching multiple target points by maneuvering a bevel-tip flexible needle can be modified to account for the avoidance of a spherical obstacle in the following way. For every needle trajectory already generated (i.e. $\widehat{P_i P_1}$, $\widehat{P_{\text{turn1}} P_2}$, and $\widehat{P_{\text{turn2}} P_3}$), we can check whether any point of that trajectory lies within the closed surface bounding an obstacle. This can be done in a similar manner to the approach described in Section 4.1, where the conditions determining the mutual position of a point and a torus in the 3D space are formulated.

To illustrate this, consider Example 2 with the same target points as in Example 1 and an additional spherical obstacle of radius $R_0 = 0.15$ placed at the point $(0.25, 0.25, 0.25)$. The results structured analogously to the ones shown in Figs. 9 and 10 are shown in Figs. 13 and 14, and the parameters of the insertion procedure are given in the column named Example 2 in Table I. The white circular areas in Figs. 13 and 14(a) represent the unfeasible insertion area due to the obstacle. In addition, the detail of the density map around the unfeasible insertion area is also changed due to the obstacle (compare Figs. 10(a) and 14(a)).

5.3. Extensions of the algorithm

In this section, extensions for the proposed needle insertion plan are discussed. The proposed algorithm can be improved to handle more than three target points, avoiding obstacles in the sense of maneuvering around them, as well as utilizing the path plan in the traditional optimization framework.

The proposed motion planning algorithm (Algorithm 1) can be extended to the case of more than three target points in the environments without obstacles as follows. For the insertion point and the first two target points selected, the two arcs corresponding to stages 3 through 6 of Algorithm 1 are generated. The turning points allowing to reach the subsequent target points in any order are sought along the arcs $\widehat{P_{\text{turn1}} P_2}$ and $\widehat{P_i P_1}$. Depending on the location of these turning points, the current order of target points might change. An example of such an order change (i.e. when points P_3 and P_4 change their positions in the target order) is presented in Fig. 15.

In Duindam *et al.*,[11] the approach for bypassing obstacles is discussed, where user intervention is combined with the motion planning algorithm. An intermediate point is introduced, and motion is

https://doi.org/10.1017/S0263574713001161 Published online by Cambridge University Press

planned from the insertion point toward the intermediate point and subsequently from the intermediate point toward the target point. In our approach, however, we are looking for the insertion point which is the part of needle configuration for reaching multiple target points such that the tissue damage is minimized. Therefore, in order to account for the presence of spherical obstacles in the sense of maneuvering around them, our approach can be modified in the following way as shown in Fig. 16. If we recall that the optimal insertion point we are searching for lies in the xy-plane, we can introduce an intermediate plane γ parallel to the xy-plane such that the distance between these two planes is the same as the z-coordinate of the center of the obstacle. The search for the intermediate optimal insertion point P_{ioi} can now be performed in the plane γ, while the region of intersection of the plane γ and the obstacle is excluded from the search domain. Once the point P_{ioi} is found, an arc intersecting the xy-plane at the insertion point P_i can be generated. Note that in this case, the arcs $\widehat{P_{\text{ioi}} P_1}$ and $\widehat{P_i P_{\text{ioi}}}$ should have a common tangent at the point P_{ioi}. Therefore, taking this condition into account, an arc of the shortest length $\widehat{P_i P_{\text{ioi}}}$ can be determined. However, the locus of the possible insertion point P_i in the xy-plane is a planar curve resulting from intersecting an arbitrarily oriented plane with a horn torus. Finally, the cost function corresponding to the length of arc $\widehat{P_i P_{\text{ioi}}}$ needs to be formulated, and the minimization problem for this cost function needs to be solved. This problem was solved in Section 4.1 of Park *et al*.[23]

6. Conclusions

We introduced a new and simple insertion plan for a flexible steerable needle with a bevel tip aiming to reach multiple target points using a single insertion point. This insertion plan exploits the experimentally verified fact that a bevel-tip flexible needle follows the path which can be approximated by a planar arc when the needle is inserted without turning. The insertion plan is based on geometric characteristics of planes and arcs in the 3D space. The insertion is executed as a series of insertions, partial retractions, turning, and new insertions toward the subsequent target points. This proposed approach allows the needle tip to reach every subsequent target point using fewer rotations than reported previously. In the examples, for three target points, the optimal insertion point, insertion direction, and target sequence were obtained with which the needle causes minimal tissue damage. It was also demonstrated how obstacle avoidance can be accounted for in a simple way. In addition, extensions of the proposed approach to more complex cases such as more than three target points and maneuvering around spherical obstacles were discussed. Based on the success of the proposed approach, several future research topics emerge such as consideration of tissue deformation, inhomogeneous tissue, *in vivo* and *ex vivo* experiments, and targeting of a cloud of targets for brachytherapy.

References

1. N. Abolhassani, R. Patel and M. Moallem, "Needle insertion into soft tissue: A survey," *Med. Eng. Phys.* **29**(4), 413–431 (2007).
2. R. Alterovitz, M. Branicky and K. Goldberg, "Motion planning under uncertainty for image-guided medical needle steering," *Int. J. Robot. Res.* **27**(11–12), 1361–1374 (2008).
3. R. Alterovitz, K. Goldberg and A. Okamura, "Planning for Steerable Bevel-Tip Needle Insertion Through 2D Soft Tissue with Obstacles," *Proceedings of IEEE International Conference on Robotics and Automation (ICRA)* (2005), pp. 1640–1645.
4. J. T. Bishoff, D. Stoianovici, B. R. Lee, J. Bauer, R. H. Taylor, L. L. Whitcomb, J. A. Cadeddu, D. Chan and L. R. Kavoussi, "RCM-PAKY: Clinical application of a new robotic system for precise needle placement," *J. Endourol.* **12**(82) (1998), S82.
5. G. Bradski and A. Kaehler, *Learning OpenCV: Computer Vision with the OpenCV Library* (O'Reilly Media, Newton, MA, 2008).
6. A. Chen and S. Vijayakumar, *Prostate Cancer* (Demos Medical, New York, NY, 2011).
7. N. Chentanez, R. Alterovitz, D. Ritchie, L. Cho, K. K. Hauser, K. Goldberg, J. R. Shewchuk and J. F. O'Brien, "Interactive simulation of surgical needle insertion and steering," *ACM Trans. Graph. (TOG)* **28**(3), 88 (2009).
8. S. P. DiMaio and S. E. Salcudean, "Needle steering and motion planning in soft tissues," *IEEE Trans. Biomed. Eng.* **52**(6), 965–974 (2005).
9. L. E. Dubins, "On curves of minimal length with a constraint on average curvature, and with prescribed initial and terminal positions and tangents," *Am. J. Math.* **79**, 497–516 (1957).

https://doi.org/10.1017/S0263574713001161 Published online by Cambridge University Press

10. V. Duindam, R. Alterovitz, S. Sastry and K. Goldberg, "Screw-Based Motion Planning for Bevel-Tip Flexible Needles in 3D Environments with Obstacles," *Proceedings of IEEE International Conference on Robotics and Automation (ICRA)* (2008) pp. 2483–2488.
11. V. Duindam, J. Xu, R. Alterovitz, S. Sastry and K. Goldberg, "Three-dimensional motion planning algorithms for steerable needles using inverse kinematics," *Int. J. Robot. Res.* **29**(7), 789–800 (2010).
12. D. Glozman and M. Shoham, "Image-guided robotic flexible needle steering," *IEEE Trans. Robot.* **23**(3), 459–467 (2007).
13. K. Hauser, R. Alterovitz, N. Chentanez, A. Okamura and K. Goldberg, "Feedback Control for Steering Needles Through 3D Deformable Tissue Using Helical Paths," *Robotics Science and Systems: Online Proceedings*. Available at: http://www.roboticsproceedings.org/rss05/p37.pdf (2009) (accessed Dec. 2, 2011) 37 p.
14. E. J. Lobaton, J. Zhang, S. Patil and R. Alterovitz, "Planning Curvature-Constrained Paths to Multiple Goals Using Circle Sampling," *Proceedings of IEEE International Conference on Robotics and Automation (ICRA)* (2011) pp. 1463–1469.
15. A. Majewicz, T. R. Wedlick, K. B. Reed and A. M. Okamura, "Evaluation of Robotic Needle Steering in *ex vivo* Tissue," *Proceedings of IEEE International Conference on Robotics and Automation (ICRA)* (2010) pp. 2068–2073.
16. V. Mallapragada, N. Sarkar and T. K. Podder, "Robot-Assisted Real-Time Tumor Manipulation for Breast Biopsy," *Proceedings of IEEE International Conference on Robotics and Automation (ICRA)* (2008) pp. 2515–2520.
17. S. Misra, K. B. Reed, B. W. Schafer, K. T. Ramesh and A. M. Okamura, "Mechanics of flexible needles robotically steered through soft tissue," *Int. J. Robot. Res.* **29**(13), 1640 (2010).
18. National Institutes of Health (NIH), Liver biopsy. Available at: `http://www.digestive.niddk.nih.gov/ddiseases/ pubs/liverbiopsy/` (accessed Dec. 2, 2011).
19. S. Okazawa, R. Ebrahimi, J. Chuang, S. E. Salcudean and R. Rohling, "Hand-held steerable needle device," *IEEE/ASME Trans. Mechatronics* **10**(3), 285–296 (2005).
20. W. Park, J. S. Kim, Y. Zhou, N. J. Cowan, A. M. Okamura and G. S. Chirikjian, "Diffusion-based Motion Planning for a Nonholonomic Flexible Needle Model," *Proceedings of IEEE International Conference on Robotics and Automation(ICRA)* (2005) pp. 4600–4605.
21. W. Park, Y. Liu, Y. Zhou, M. Moses and G. S. Chirikjian, "Kinematic state estimation and motion planning for stochastic nonholonomic systems using the exponential map," *Robotica* **26**(4), 419–434 (2008).
22. W. Park, K. B. Reed, A. M. Okamura and G. S. Chirikjian, "Estimation of Model Parameters for Steerable Needles," *Proceedings of IEEE International Conference on Robotics and Automation (ICRA)* (2010) pp. 3703–3708.
23. W. Park, Y. Wang and G. S. Chirikjian, "The path-of-probability algorithm for steering and feedback control of flexible needles," *Int. J. Robot. Res.* **29**(7), 813 (2010).
24. K. B. Reed, A. Majewicz, V. Kallem, R. Alterovitz, K. Goldberg, N. J. Cowan and A. M. Okamura, "Robot-assisted needle steering," *Robot. Autom. Mag. IEEE* **18**(4), 35–46 (2011).
25. K. B. Reed, A. M. Okamura and N. J. Cowan, "Modeling and control of needles with torsional friction," *IEEE Trans. Biomed. Eng.* **56**(12), 2905–2916 (2009).
26. K. B. Reed, V. Kallem, R. Alterovitz, K. Goldberg, A. M. Okamura and N. J. Cowan, "Integrated Planning and Image-Guided Control for Planar Needle Steering," *Proceedings of IEEE/RAS-EMBS International Conference on Biomedical Robotics and Biomechatronics (BioRob)* (2008) pp. 819–824.
27. P. R. Rizun, P. B. McBeth, D. F. Louw and G. R. Sutherland, "Robot-assisted neurosurgery," *Semin. Laparosc. Surg.* **11**(2), 99–106 (2004).
28. R. Szeliski, *Computer Vision: Algorithms and Applications* (Springer, New York, NY, 2010).
29. M. Torabi, K. Hauser, R. Alterovitz, V. Duindam and K. Goldberg, "Guiding Medical Needles Using Single-Point Tissue Manipulation," *Proceedings of IEEE International Conference on Robotics and Automation (ICRA)* (2009), pp. 2705–2710.
30. R. J. Webster III, J. Memisevic and A. M. Okamura, "Design Considerations for Robotic Needle Steering," *Proceedings of IEEE International Conference on Robotics and Automation (ICRA)* (2005) pp. 3588–3594.
31. R. J. Webster III, J. S. Kim, N. J. Cowan, G. S. Chirikjian and A. M. Okamura, "Nonholonomic modeling of needle steering," *Int. J. Robot. Res.* **25**(5–6), 509–525 (2006).
32. Z. Wei, G. Wan, L. Gardi, G. Mills, D. Downey and A. Fenster, "Robot-assisted 3D-TRUS-guided prostate brachytherapy: System integration and validation," *Med. Phys.* **31**(3), 539–548 (2004).
33. J. Xu, V. Duindam, R. Alterovitz, J. Pouliot, J. A. M. Cunha, I. C. Hsu and K. Goldberg, "Planning "Fireworks" Trajectories for Steerable Medical Needles to Reduce Patient Trauma," *Proceedings of IEEE/RSJ International Conference on Intelligent Robots and Systems (IROS)* (2009) pp. 4517–4522.
34. A. Zivanovic and B. L. Davies, "A robotic system for blood sampling," *IEEE Trans. Inform. Technol. Biomed.* **4**(1), 8–14 (2000).

Appendix: Experiments

The experimental setup we used to support the idea that the path of the beveled tip of a flexible needle is approximated by a circle of *small* curvature is shown in Fig. 17. The system we built consists of

https://doi.org/10.1017/S0263574713001161 Published online by Cambridge University Press

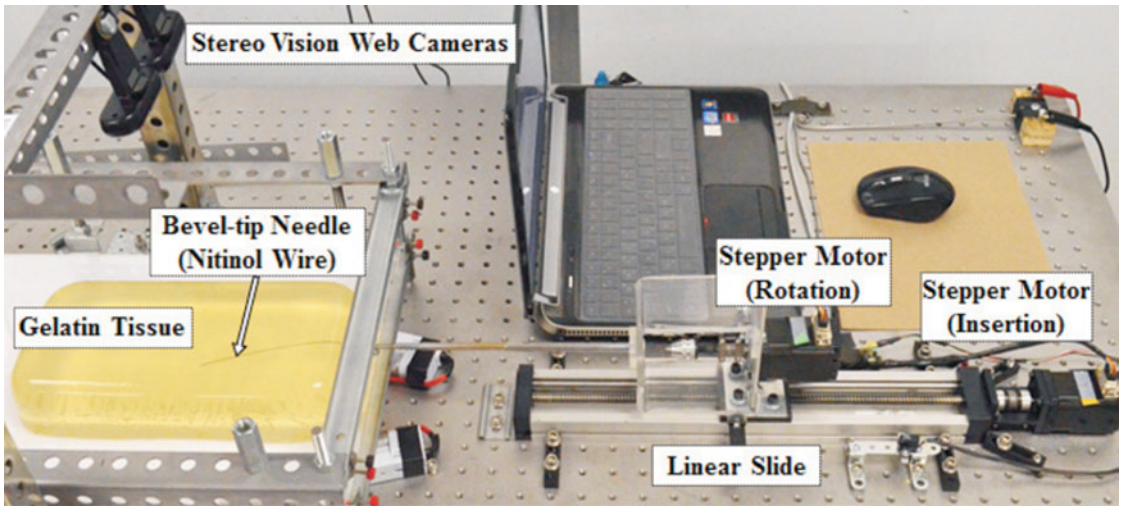

Fig. 17. (Colour online) The experimental setup for needle insertion.

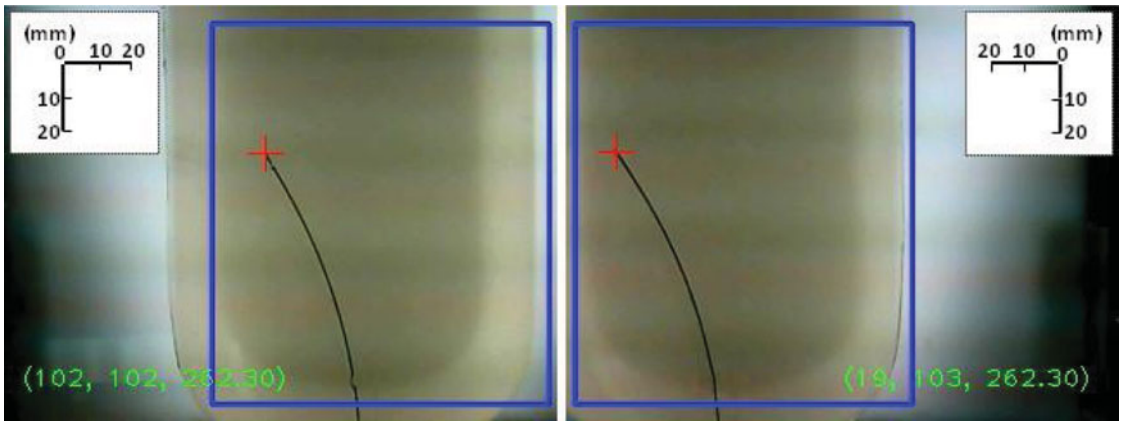

Fig. 18. (Colour online) The insertion results captured by stereo vision.

two stepper motors, a phantom tissue, and a Nitinol wire as a substitute for a flexible needle. One stepper motor drives the linear slide to insert the needle into the phantom tissue, while the other one located on the top of the linear slide rotates the needle shaft. The stepper motors are operated via RS-485 communication protocol and have 1.8^{o} in each rotation step, also partitioned into 256 microsteps. The phantom tissue was made from clear gelatin sheets mixed with powder sugar for sufficient transparency and hardness. The Nitinol wire (Nitinol Devices and Components, Fremont, CA) we used has a 0.71-mm (0.028-in) diameter and a bevel angle of roughly 45^{o}. In order to prevent unexpected bending and buckling during insertion, the Nitinol wire is enclosed within a support sheath outside the artificial tissue.

A pair of C210 web cameras (Logitech, Morges, Switzerland) were mounted above the artificial tissue perpendicular to its plane of vertical symmetry in order to obtain the 3D coordinates of the needle tip. For this purpose, a pair of images captured by two cameras were processed using the Epipolar (Stereo) Geometry[5,28] approach, which resulted in the Cartesian coordinate accuracy of 1 mm. The dimensions of the phantom tissue are $140 \times 280 \times 40$ mm, its transparency is sufficient to identify the needle tip by means of a pair of web cameras, and its top surface is assumed to be horizontal, for which its support plate was appropriately leveled.

The insertion procedure was accomplished by motor control software programmed in C# language using Visual Studio 2010. The needle was inserted to the total depth of 130 mm with a 10-mm step at

https://doi.org/10.1017/S0263574713001161 Published online by Cambridge University Press

the constant rotation angle. Using 13 sets of coordinates of the needle tip and fitting a circle through the points with these coordinates, we obtained the circle radius of approximately 203 mm. In Fig. 18, the insertion results captured by both left and right web cameras with 110-mm insertion depth and 203-mm radius of curvature (corresponding to the curvature $\kappa = 0.0043$) are shown. A rectangle in the image indicates the detecting area to avoid image noise, and three numbers represent the 3D coordinates of the needle tip in millimeters.

https://doi.org/10.1017/S0263574713001161 Published online by Cambridge University Press